UC Santa Barbara
UC Santa Barbara Previously Published Works

Title
High-temperature phase stability of hafnium aluminate films for alternative gate dielectrics

Permalink
https://escholarship.org/uc/item/4mx9p5k5

Journal
Journal of Applied Physics, 95(7)

ISSN
0021-8979

Authors
Yang, Y
Zhu, W J
Ma, T P
et al.

Publication Date
2004-04-01

Peer reviewed

eScholarship.org Powered by the California Digital Library
University of California

High-temperature phase stability of hafnium aluminate films for alternative gate dielectrics

Yan Yang

Materials Department, University of California, Santa Barbara, CA 93106-5050, U.S.A.

Wenjuan Zhu[a] and T.P. Ma

Department of Electrical Engineering, Yale University, New Haven, CT 06520, U.S.A.

Susanne Stemmer[b]

Materials Department, University of California, Santa Barbara, CA 93106-5050, U.S.A.

[a] present address: IBM Microelectronics, 2070 Route 52, M/S: E40, Hopewell Junction, NY 12533, U.S.A.

[b] Corresponding author. Electronic mail: stemmer@mrl.ucsb.edu

ABSTRACT

Hafnium aluminate films with different compositions were deposited at room temperature by jet vapor deposition. The as-deposited films were amorphous. After annealing at 1100 °C, the microstructure of the films was analyzed by high-resolution transmission electron microscopy, electron diffraction and electron energy loss spectroscopy (EELS). The crystalline phase in pure HfO_2 films was monoclinic. With increasing Al content in the films, the amount of metastable HfO_2 with a tetragonal distorted fluorite structure increased. In addition, the grain sizes decreased, making the detection of crystallization by x-ray diffraction difficult. No crystalline Al_2O_3 phase could be unambiguously detected in electron diffraction patterns in films with up to 30 mol% Al_2O_3. However, an Al-rich intergranular phase was identified by EELS. Films with ~ 64 mol% Al_2O_3 crystallized as tetragonal HfO_2 and metastable cubic Al_2O_3 with the spinel structure. The complex microstructures of the films should be considered in the interpretation of their dielectric and electrical properties after high temperature anneals.

INTRODUCTION

Thin films of transition metal oxides with dielectric constants (*k*) greater than that of SiO_2 (k_{SiO_2} = 3.9) are currently being investigated as novel gate dielectric materials in complementary metal-oxide-semiconductor (CMOS) devices. High-*k* metal oxides that are potentially stable in contact with Si include HfO_2 and ZrO_2, and their alloys with SiO_2 (silicates) and Al_2O_3 (aluminates), respectively [1-4]. Device processing requires temperatures around 1000 °C, and it is now well established that amorphous Hf- or Zr-silicate films phase separate at high temperatures into a silica-rich and a transition metal (Hf or Zr)-oxide-rich phase [5-9]. Phase separation produces local variations in the dielectric properties of the films that may be detrimental for devices, for example by causing electric field variations in the underlying Si channel [7]. In contrast, less is known about the phase stability of thin film aluminates.

The HfO_2-Al_2O_3 phase diagram is not completely developed (Fig. 1) [10]. In contrast, the ZrO_2-Al_2O_3 phase diagram is well established [11]. HfO_2 and ZrO_2 are chemically similar. Both HfO_2 and ZrO_2 have three polymorphs that are based on the cubic fluorite structure: cubic, tetragonal (*t*) and monoclinic (*m*), which is the stable phase at room temperature. The temperature of the monoclinic to tetragonal phase transformation is about 700 °C higher in HfO_2 (~ 1700 °C) than in ZrO_2 [12]. The tetragonal (or cubic) phase can be retained ("stabilized") at room temperature by alloying with cations with lower valence that substitute for M^{4+} (M = Zr or Hf) [12]. The equilibrium solubility of α-Al_2O_3 (corundum) in *m*-ZrO_2 is small (< 1 mol%) and the solubility of ZrO_2 in α-Al_2O_3 is negligible [11,13,14]. The low mutual solubility has

been attributed to the size of Al^{3+}, which is apparently too small to substitute for Zr^{4+}, and the absence of suitably sized interstitial sites for Zr^{4+} in the corundum structure, respectively [15]. Similar low equilibrium solubilities are expected in the HfO_2-Al_2O_3 system.

Several studies have reported the crystallization of metastable phases with highly extended solid solubilities in the ZrO_2-Al_2O_3 system [15,16]. Metastable phases form during the annealing of amorphous phases when the equilibrium phase assembly is kinetically suppressed [17]. The intermediate, crystalline metastable phases lower the free energy of the system, although not as much as the equilibrium phases. The metastable phases are often structurally less complex or more tolerant of disorder and nonstoichiometry than the equilibrium phases and thus are kinetically favored [17]. Al_2O_3 in particular forms a large number of metastable polymorphs [18]. Impurities, defects or large surface areas may also lead to the formation of metastable polymorphs. The following transformation sequence has been reported in the literature for the pyrolysis of ZrO_2-Al_2O_3 precursors [15,19]:

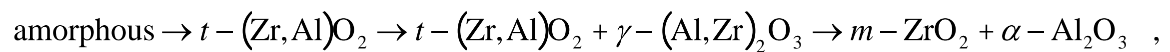

$$\text{amorphous} \rightarrow t-(\text{Zr,Al})\text{O}_2 \rightarrow t-(\text{Zr,Al})\text{O}_2 + \gamma-(\text{Al,Zr})_2\text{O}_3 \rightarrow m-\text{ZrO}_2 + \alpha-\text{Al}_2\text{O}_3 \quad ,$$

where γ denotes Al_2O_3 with the cubic spinel structure. Samples with up to 40 mol% of Al_2O_3 were reported to crystallize single-phase tetragonal ZrO_2 with Al in solid solution (denoted t-(Zr,Al)O_2 above) [15], i.e., a large, metastable solubility for Al_2O_3 was claimed. Tetragonal or cubic ZrO_2 were also the crystalline phases observed in annealing studies of thin film ZrO_2-Al_2O_3 for gate dielectrics [20,21]. For high Al_2O_3 concentrations, films were reported to remain amorphous under typical device annealing

conditions [3]. One of the goals of this paper is to investigate whether extended metastable solubilities exist in HfO_2-Al_2O_3 films after high temperature anneals necessary for CMOS device processing. HfO_2 is more difficult to stabilize than ZrO_2 [12] and thus one may also expect less extended solubilities.

X-ray diffraction studies alone are insufficient to establish the microstructure of these ultrathin films, as amorphous or crystalline phases with small grain sizes or a high concentration of defects are difficult to detect. In this paper, we used a combination of high-resolution transmission electron microscopy (HRTEM), electron diffraction and electron energy-loss spectroscopy (EELS) to investigate the microstructure and accommodation of Al in HfO_2-Al_2O_3 thin film alloys with different compositions after high temperature anneals.

EXPERIMENTAL

$(HfO_2)_{1-x}(Al_2O_3)_x$ films with different compositions x were deposited by jet vapor-deposition (JVD) at room temperature on HF-last Si substrates. Hf, Al and O_2 vapors were generated by dc sputtering in separate nozzles and brought into the deposition chamber by a supersonic Ar jet. Details of the deposition process are described elsewhere [4,22]. Al/(Hf+Al) ratios ($x_{at\%}$) were determined by x-ray photoelectron spectroscopy and used to estimate the mol% of Al_2O_3 (or x) in the formula above (i.e., $x = x_{at\%} / (2 - x_{at\%})$). The five films investigated in this paper had Al/(Hf+Al) ratios that corresponded to x = 0, 0.07, 0.30, 0.64 and 1.0, respectively. The film thickness was about 80 nm. Films were amorphous (or quasi-amorphous [23]) after deposition [24].

All samples were annealed at 1100 °C for 2 min in flowing N_2. Grazing incidence x-ray diffraction (XRD) did not detect any crystallization in the pure Al_2O_3 film and the film with $x = 0.64$. XRD detected peaks after annealing at 325±25 °C in pure HfO_2, at 725±25 °C for the film with $x = 0.07$ and at 1000±25 °C for the film with $x = 0.30$. Plan-view transmission electron microscopy (TEM) samples were prepared by standard techniques, with Ar ion-milling as a final step. HRTEM was performed using transmission electron microscopes operating at 200 kV (JEOL JEM2010 and JEM 2010F, respectively). Selected area electron diffraction (SAD) patterns were recorded using the JEM2010. EELS line scans were obtained in the JEM 2010F, which is equipped with a field-emission gun, annular dark-field detectors and a post-column imaging filter (Gatan GIF200). This microscope is capable of achieving sub-0.2 nm probe sizes in scanning transmission electron microscopy (STEM) for microanalysis and incoherent Z-contrast lattice imaging [25]. The probe size used for EELS was about 0.2 nm.

RESULTS AND DISCUSSION

The insets in Fig. 2 show SAD patterns obtained from plan-view samples of the HfO_2 film (Fig. 2a), of the HfO_2-Al_2O_3 films with different compositions (Fig. 2b-d), and of the Al_2O_3 film (Fig. 2e) after annealing at 1100 °C. All patterns showed well-defined rings, indicating that all films were polycrystalline. Table 1 summarizes the lattice plane spacings measured for the five samples and compares them with those reported for bulk *m*-HfO_2, *t*-HfO_2 and γ-Al_2O_3.

The patterns showed that even the films with x = 1.0 and x = 0.64, which exhibited no detectable peaks in XRD, had crystallized. The absence of peaks in XRD is likely due to the small grain size of these films (< 5 nm) and the highly defective nature of the Al_2O_3 film (see Fig. 2e), which causes broadening of the reflections in XRD, making them difficult to detect. The crystalline phase of the pure HfO_2 film ($x = 0$) was the low-temperature equilibrium monoclinic polymorph. No twinning, which would be characteristic of the $t \rightarrow m$ phase transformation, could be detected in this film. Thus the films nucleated as monoclinic HfO_2. The grain sizes in this film were about 10 – 15 nm (Fig. 2a).

The lattice plane spacings in the pure Al_2O_3 film ($x = 1.0$) could be assigned to the cubic spinel (γ) structure, rather than the equilibrium corundum (α) structure. Other authors have observed that the initial crystallizing phase during heating of amorphous Al_2O_3 films was γ-Al_2O_3 even in cases where films were templated by an α-Al_2O_3 substrate that should promote the nucleation of corundum [26]. In α-Al_2O_3, the oxygen anions form a hexagonal close-packed (hcp) arrangement, whereas in cubic spinel they form a face-centered cubic (fcc) arrangement. The cations in γ-Al_2O_3 are partially disordered [18]. LEVI suggested that the absence of sufficient time for ordering during crystallization favors the spinel structure over the corundum structure [17]. Crystallization to α-Al_2O_3 would require that the Al ions form a regular pattern in the interstitial sites of the O close packed layers, and γ-Al_2O_3 may thus become energetically favored over an α-Al_2O_3 film containing a high density of defects [17]. In addition, the rearrangement of oxygen anions may also be rate limiting during crystallization from the

amorphous phase [27]. Consistent with both mechanisms, long annealing times are known to cause the transformation to the equilibrium α-phase [26].

The diffraction rings in the films with 7 mol% Al_2O_3 (Fig. 2b) and with 30 mol% Al_2O_3 (Fig. 2c) could be indexed as a mixture of monoclinic and tetragonal HfO_2. Diffraction rings corresponding to lattice planes spacings of m-HfO_2, i.e. ~ 3.68 Å, had a reduced relative intensity and some of the monoclinic spacings were missing in the patterns as the Al-content was increased (see Table I). No reflections that could be unambiguously assigned to any of the crystalline phases of Al_2O_3 could be detected in these two films, although γ-Al_2O_3 may be difficult to detect in the presence of m-HfO_2. Therefore, as discussed below, EELS was used to further investigate whether additional phases were present. In the film with 64 mol% Al_2O_3, the characteristic monoclinic lattice plane spacing of ~3.68Å could not be detected. However, measured lattice plane spacings matched well with γ-Al_2O_3. Therefore, the crystallizing phases in the film with 64 mol% Al_2O_3 were t-$(Hf,Al)O_2$ and γ-$(Al,Hf)_2O_3$. This is consistent with the observations by BALMER *et al.* for high Al_2O_3 concentrations in ZrO_2-Al_2O_3 alloys [15]. It is possible that a greater driving force for transformation to γ-Al_2O_3 exists at high Al_2O_3 contents [15]. The **crystallizing** phases for the different film compositions are shown in Fig. 1.

Figure 2 also shows HRTEM images obtained from the five films. With increasing amount of Al_2O_3, the grain sizes decreased, from about 5 – 20 nm in film with 7 mol% Al_2O_3, to ~ 5 nm in the film with 30 mol% Al_2O_3 and 3 - 5 nm in the film with 64 mol% Al_2O_3. The grain size in the pure Al_2O_3 film was difficult to determine, due to a

high concentration of defects, although lattice fringes are visible in the HRTEM image of this sample and the electron diffraction pattern showed that the films were clearly crystalline. All alloyed films also contained some amorphous or poorly crystallized phase.

With respect to the accommodation of Al in the films, the presence of *t*-HfO_2 in the films with 7 – 64 mol% Al_2O_3 indicated that some Al was accommodated in solid solution in the crystallizing HfO_2, where it stabilized the tetragonal phase. Similar to other trivalent or divalent ions, small amounts of Al^{3+} may substitute for Hf^{4+} and stabilize the tetragonal phase, such as Y^{3+} or Ca^{2+}. However, in contrast to metastable ZrO_2-Al_2O_3 alloys, which have been reported in the literature to crystallize to a single *t*-(Zr,Al)O_2 phase [15], the monoclinic phase could still be detected in Hf-aluminate films with up to ~ 30 mol% Al_2O_3. The absence of twinning indicated that this monoclinic phase had not formed by transformation of tetragonal grains. Very large amounts of Al_2O_3 (> 30 mol%) were needed to obtain only *t*-HfO_2 in the films, thus Al is not a very efficient stabilizer. Furthermore, the very small grain size in the sample with 64 mol% Al_2O_3 may also have contributed to the stabilization of the tetragonal phase [12,28]. Thus, most of the excess Al is likely accommodated as grain boundary phase in these films even before crystalline Al_2O_3 can be detected by electron diffraction.

Other authors have observed segregation of Al to the grain boundaries in ZrO_2 doped with 0.15 wt% of Al_2O_3 [29]. To further investigate the accommodation of Al, EELS line scans of the Al $L_{2,3}$-edges (79 eV) were performed across several grains. It should be noted that in the heavily elastically scattering HfO_2-rich grains reduced the

intensity of the EELS spectra, making the amount of Al was difficult to quantify in these grains [30]. Figure 3 shows an Al profile, as calculated from the intensity under the Al $L_{2,3}$-edge, for the film with ~ 30 mol% Al_2O_3, and the corresponding high-angle annular dark-field (HAADF) image that was used to position the scan. The Hf(Al)O_2 grains appear bright in Fig. 3a whereas the darker areas are the intergranular phase. The contrast is due to the strong atomic number sensitivity of the HAADF imaging technique. As can be seen from Fig. 3b, the concentration of Al was significantly higher if the electron probe was located between the Hf(Al)O_2 grains. Thus the phase assembly in the film with 30 mol% Al_2O_3 was more accurately described as *m*-HfO_2 + *t*-(Hf,Al)O_2 + *gb*-Al(Hf)-O, where *gb*-Al(Hf)-O represents the intergranular Al-rich phase, which is amorphous or poorly crystallized. The presence of monoclinic HfO_2 and the Al-rich intergranular phase in the film with 30 mol% Al_2O_3 showed that the metastable solubilities in this system are small at 1100 °C.

CONCLUSIONS

In summary, thin film HfO_2-Al_2O_3 alloys that are candidates for alternative gate dielectrics and that are subjected to high-temperature anneals showed complex microstructures. Many of the crystallizing phases after these relatively short annealing times were metastable phases, such as γ-Al_2O_3 and tetragonal HfO_2. Films with up to 30 mol% Al_2O_3 did not form crystalline Al_2O_3 within the detection limit. Excess Al was accommodated as an amorphous or poorly crystalline intergranular phase, where it may influence the electrical and dielectric properties of the film, as well as the stability of the

films against reactions, such as with the polycrystalline Si gate electrode [31]. The results demonstrated that high-spatial resolution TEM techniques are required to obtain a complete understanding of the microstructure. Future studies should be directed towards establishing the structure-property relationships for these films.

ACKNOWLEDGMENTS

This work was supported by the SRC/iSematech Front End Process Center. The authors are grateful to Dr. Zhiqiang Chen for preparing some of the TEM samples and for recording the HRTEM image shown in Fig. 2a. The use of the STEM (JEOL 2010F) at the RRC at the University of Illinois at Chicago is gratefully acknowledged. This work made use of the MRL Central Facilities supported by NSF under Award No. DMR 00-80034.

REFERENCES

[1] G. D. Wilk, R. M. Wallace, and J. M. Anthony, J. Appl. Phys. **87,** 484 (2000).

[2] W. J. Zhu, T. P. Ma, T. Tamagawa, Y. Di, J. Kim, R. Carruthers, M. Gibson, and T. Furukawa, IEDM Technical Digest**,** 20 (2001).

[3] M. Y. Ho, H. Gong, G. D. Wilk, B. W. Busch, M. L. Green, W. H. Lin, A. See, S. K. Lahiri, M. E. Loomans, P. I. Raisanen, and T. Gustafsson, Appl. Phys. Lett. **81,** 4218 (2002).

[4] W. J. Zhu, T. Tamagawa, M. Gibson, T. Furukawa, and T. P. Ma, IEEE Electron Dev. Lett. **23,** 649 (2002).

[5] S. Stemmer, Z. Q. Chen, C. G. Levi, P. S. Lysaght, B. Foran, J. A. Gisby, and J. R. Taylor, Jap. J. Appl. Phys. Part 1 **42,** 3593 (2003).

[6] G. Rayner, R. Therrien, and G. Lucovsky, Mat. Res. Soc. Symp. **611,** C1.3.1 (2000).

[7] S. Stemmer, Y. Lu, B. Foran, P. S. Lysaght, S. K. Streiffer, P. Fuoss, and S. Seifert, Appl. Phys. Lett. **83,** 3141 (2003).

[8] H. Kim and P. C. McIntyre, J. Appl. Phys. **92,** 5094 (2002).

[9] J. P. Maria, D. Wicaksana, A. I. Kingon, B. Busch, H. Schulte, E. Garfunkel, and T. Gustafsson, J. Appl. Phys. **90,** 3476 (2001).

[10] V. A. Lysenko, Inorg. Mater. **30,** 930 (1994).

[11] *Phase Diagrams for Zirconium and Zirconia Systems*; *Vol.*, edited by H. M. Ondik and H. F. McMurdie (The American Ceramic Society, 1998).

[12] J. Wang, H. P. Li, and R. Stevens, J. Mater. Sci. **27,** 5397 (1992).

[13] S. Popovic, G. Stefanic, and S. Music, Mater. Lett. **31,** 19 (1997).

[14] S. M. Alper, in *Science of Ceramics*; *Vol. 3* (Academic Press, London, 1967), p. 335.

[15] M. L. Balmer, F. F. Lange, and C. G. Levi, J. Amer. Ceram. Soc. **77,** 2069 (1994).

[16] S. Moreau, M. Gervais, and A. Douy, Solid State Ionics **101,** 625 (1997).

[17] C. G. Levi, Acta Mater. **46,** 787 (1998).

[18] I. Levin and D. Brandon, J. Am. Ceram. Soc. **81,** 1995 (1998).

[19] P. K. Narwankar, J. S. Speck, and F. F. Lange, J. Mater. Res. **10,** 1756 (1995).

[20] R. B. van Dover, D. V. Lang, M. L. Green, and L. Manchanda, J. Vac. Sci. & Technol. A **19,** 2779 (2001).

[21] C. Zhao, O. Richard, E. Young, H. Bender, G. Roebben, S. Haukka, S. De Gendt, M. Houssa, R. Carter, W. Tsai, O. Van ber Biest, and M. Heyns, J. Non-Cryst. Sol. **303,** 144 (2002).

[22] T. P. Ma, IEEE Trans. Electron Devices **45,** 680 (1998).

[23] M. Y. Ho, H. Gong, G. D. Wilk, B. W. Busch, M. L. Green, P. M. Voyles, D. A. Muller, M. Bude, W. H. Lin, A. See, M. E. Loomans, S. K. Lahiri, and P. I. Raisanen, J. Appl. Phys. **93,** 1477 (2003).

[24] S. Stemmer, Z. Q. Chen, W. J. Zhu, and T. P. Ma, J. Microscopy-Oxford **210,** 74 (2003).

[25] E. M. James, N. D. Browning, A. W. Nicholls, M. Kawasaki, Y. Xin, and S. Stemmer, J. Electron Micros. **47,** 561 (1998).

[26] N. Yu, Q. Wen, D. R. Clarke, P. C. McIntyre, H. Kung, M. Nastasi, T. W. Simpson, I. V. Mitchell, and D. Q. Li, J. Appl. Phys. **78,** 5412 (1995).

[27] T. W. Simpson, Q. Wen, N. Yu, and D. R. Clarke, J. Am. Ceram. Soc. **81,** 61 (1998).

[28] R. C. Garvie, J. Phys. Chem. **69,** 1238 (1965).

[29] I. M. Ross, W. M. Rainforth, D. W. McComb, A. J. Scott, and R. Brydson, Scripta Mater. **45,** 653 (2001).

[30] B. Foran, J. Barnett, P. S. Lysaght, M. P. Agustin, and S. Stemmer, submitted to: J. Electron Spectrosc.

[31] D. C. Gilmer, R. Hegde, R. Cotton, R. Garcia, V. Dhandapani, D. Triyoso, D. Roan, A. Franke, R. Rai, L. Prabhu, C. Hobbs, J. M. Grant, L. La, S. Samavedam, B. Taylor, H. Tseng, and P. Tobin, Appl. Phys. Lett. **81,** 1288 (2002).

Table I: Bulk lattice plane spacings as listed in the powder diffraction files (JCPDS) for m-HfO_2, t-HfO_2 and γ-Al_2O_3 and measured spacings for the different films. All plane spacings are given in Å. The bulk lattice spacings are listed down to the smallest spacings that were measured. For m-HfO_2 the smaller spacings are very close together and are not listed. For the films with x > 0, spacings larger than ~ 4.6 Å could not be measured in these experiments (see Fig. 2).

<table>
<tr><th>m-HfO_2[a]</th><th>t-HfO_2[b]</th><th>γ-Al_2O_3[c]</th><th>$x = 0$</th><th>$x = 0.07$</th><th>$x = 0.30$</th><th>$x = 0.64$</th><th>$x = 1.0$</th></tr>
<tr><td>5.05 - 5.07</td><td></td><td></td><td>5.06</td><td></td><td></td><td></td><td></td></tr>
<tr><td></td><td></td><td>4.56</td><td></td><td></td><td></td><td></td><td>4.57</td></tr>
<tr><td>3.61 - 3.68</td><td></td><td></td><td>3.63</td><td>3.67</td><td>3.67</td><td></td><td></td></tr>
<tr><td>3.15</td><td></td><td></td><td>3.06 – 3.23</td><td></td><td></td><td></td><td></td></tr>
<tr><td></td><td>2.97</td><td></td><td></td><td>2.91 – 3.03</td><td>2.89-3.06</td><td>2.86-3.03</td><td></td></tr>
<tr><td>2.82</td><td></td><td>2.8</td><td>2.82</td><td></td><td></td><td></td><td>2.82</td></tr>
<tr><td>2.59 – 2.61</td><td>2.622</td><td></td><td rowspan="3">2.48 – 2.62 [d]</td><td rowspan="2">2.51 – 2.69</td><td rowspan="3">2.48-2.61 [d]</td><td></td><td></td></tr>
<tr><td>2.52 - 2.53</td><td>2.555</td><td></td><td rowspan="3">2.35-2.51 [d]</td><td></td></tr>
<tr><td>2.48 – 2.49</td><td></td><td></td><td></td><td rowspan="2">2.36-2.48</td></tr>
<tr><td>2.32</td><td>2.356</td><td>2.39</td><td></td><td></td><td></td></tr>
<tr><td>2.2</td><td></td><td>2.28</td><td rowspan="2">2.19 – 2.27 [d]</td><td></td><td></td><td></td><td>2.27</td></tr>
<tr><td>2.17</td><td></td><td></td><td>2.11</td><td>2.12</td><td></td><td></td></tr>
<tr><td>2.01</td><td></td><td></td><td></td><td></td><td></td><td></td><td rowspan="2">1.94-2.01 [d]</td></tr>
<tr><td>1.98</td><td></td><td>1.97</td><td>1.97</td><td></td><td></td><td>1.98</td></tr>
<tr><td>1.84</td><td>1.837</td><td></td><td rowspan="3">1.76 – 1.83 [d]</td><td rowspan="3">1.76 – 1.83</td><td rowspan="3">1.77-1.85 [d]</td><td rowspan="3">1.77-1.84 [d]</td><td></td></tr>
<tr><td>1.79-1.81</td><td>1.811</td><td></td><td></td></tr>
<tr><td>1.77</td><td></td><td></td><td></td></tr>
<tr><td>1.63 - 1.68</td><td></td><td></td><td></td><td></td><td></td><td></td><td></td></tr>
</table>

1.58 – 1.60	1.578				1.60		
1.53	1.548	1.52		1.53		1.53	1.53
1.47–1.50	1.497					1.49	
1.44-1.35		1.395		1.40		1.40	1.40
	1.28			1.28	1.28		
	1.172 - 1.194			1.15 – 1.19	1.15-1.19		1.2
	1.154	1.14					1.14
	1.053			1.04			

[a] JCPDS #43-1017, #6-318, #34-104 (the range of spacings given reflects the differences in the reported data)

[b] JCPDS #8-342

[c] JCPDS #10-425

[d] Several rings close together or broad rings

FIGURE CAPTIONS

Figure 1

Schematic of the HfO_2-Al_2O_3 phase diagram, redrawn after [10]. The symbols represent the **crystalline** phases identified by electron diffraction in the films with different amounts of Al_2O_3 after annealing at 1100 °C.

Figure 2

Plan-view HRTEM images of HfO_2-Al_2O_3 films with different compositions: (a) pure HfO_2, (b) $(HfO_2)_{0.93}(Al_2O_3)_{0.07}$, (c) $(HfO_2)_{0.70}(Al_2O_3)_{0.30}$, (d) $(HfO_2)_{0.36}(Al_2O_3)_{0.64}$, and (e) pure Al_2O_3. The insets show SAD patterns obtained from the samples. The sharp diffraction spots are due to the underlying Si substrate not removed by ion-milling in the areas where the diffraction patterns were recorded.

Figure 3

(a) Low-magnification plan-view Z-contrast image of the film with composition $(HfO_2)_{0.70}(Al_2O_3)_{0.30}$. (b) Al concentration profile along the dotted line shown in (a), obtained from the intensity underneath the Al $L_{2,3}$ edge in EELS.

Figure 1

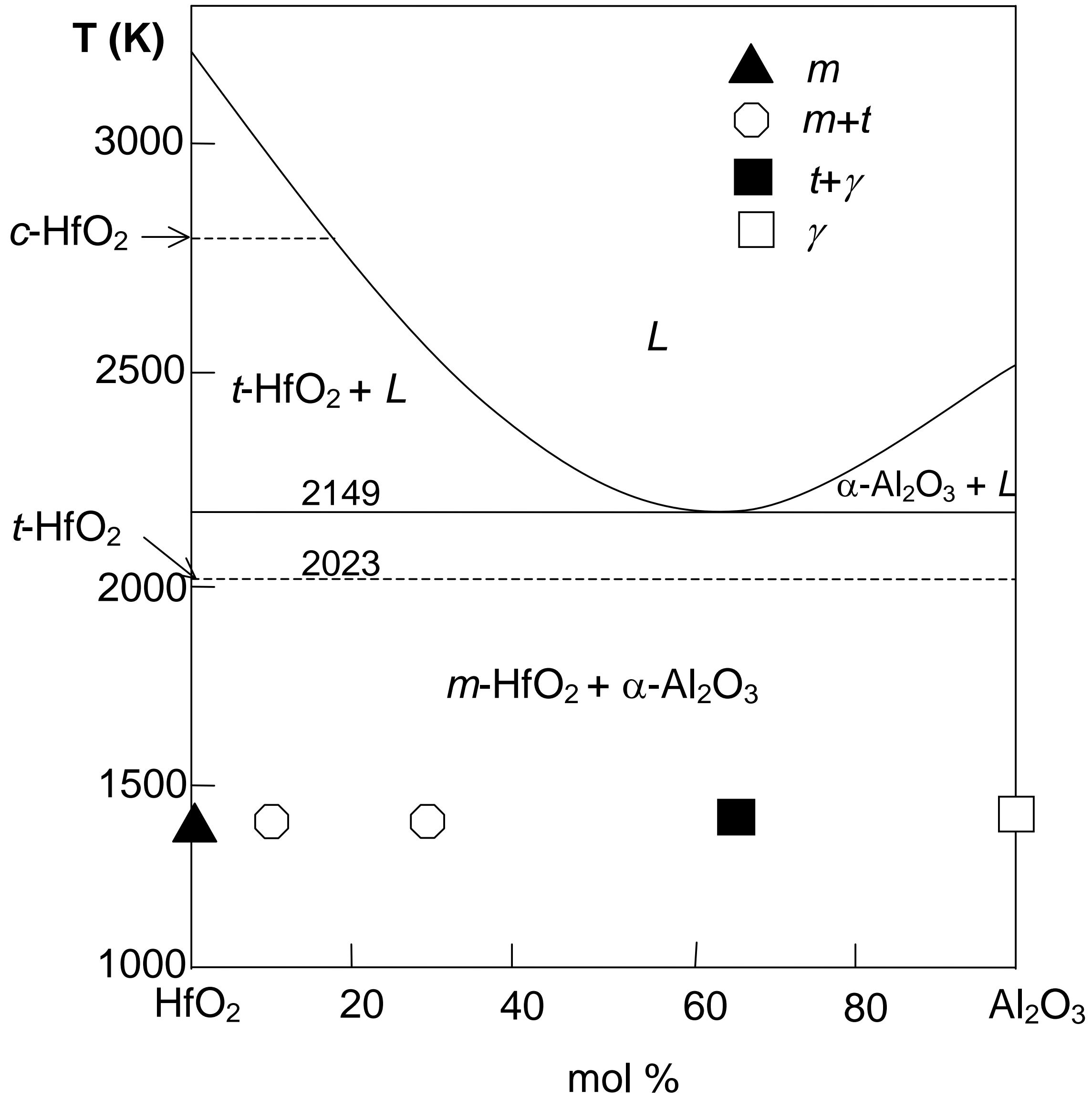

Yang *et al.*, Figure 1

Figure 2 (a)

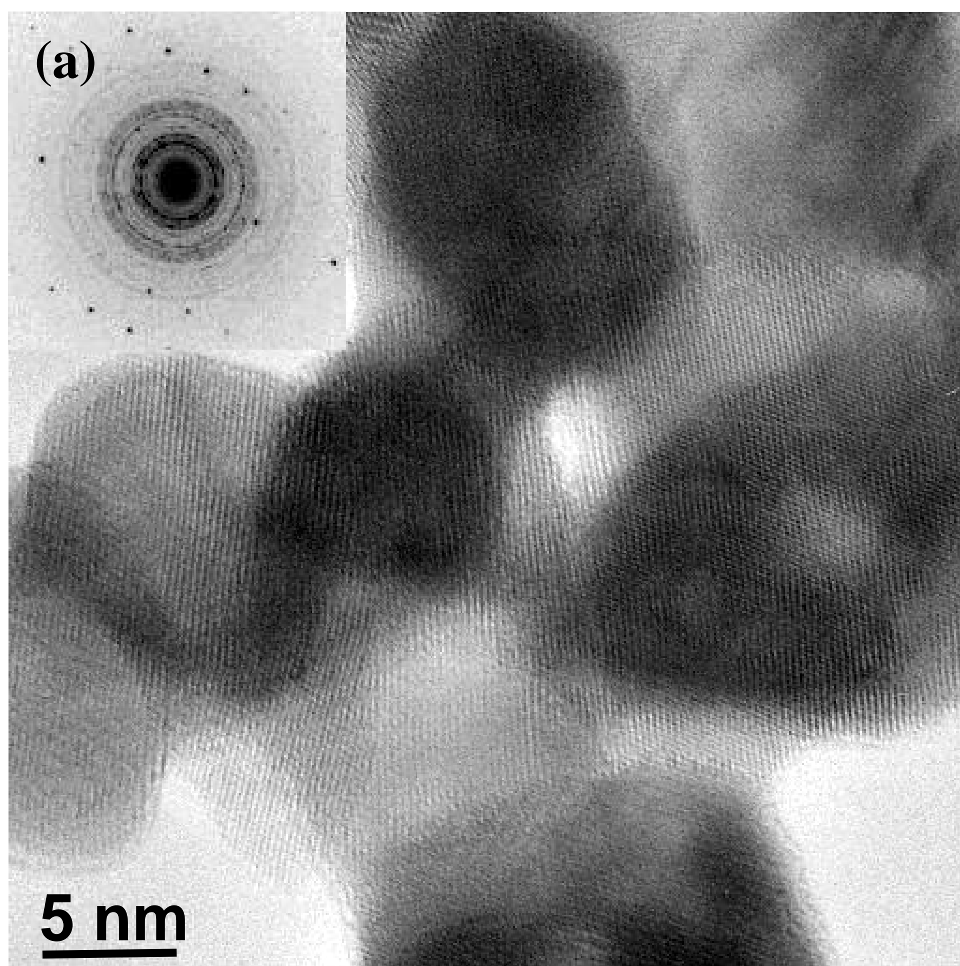

Yang *et al.*, Figure 2a

Figure 2 (b)

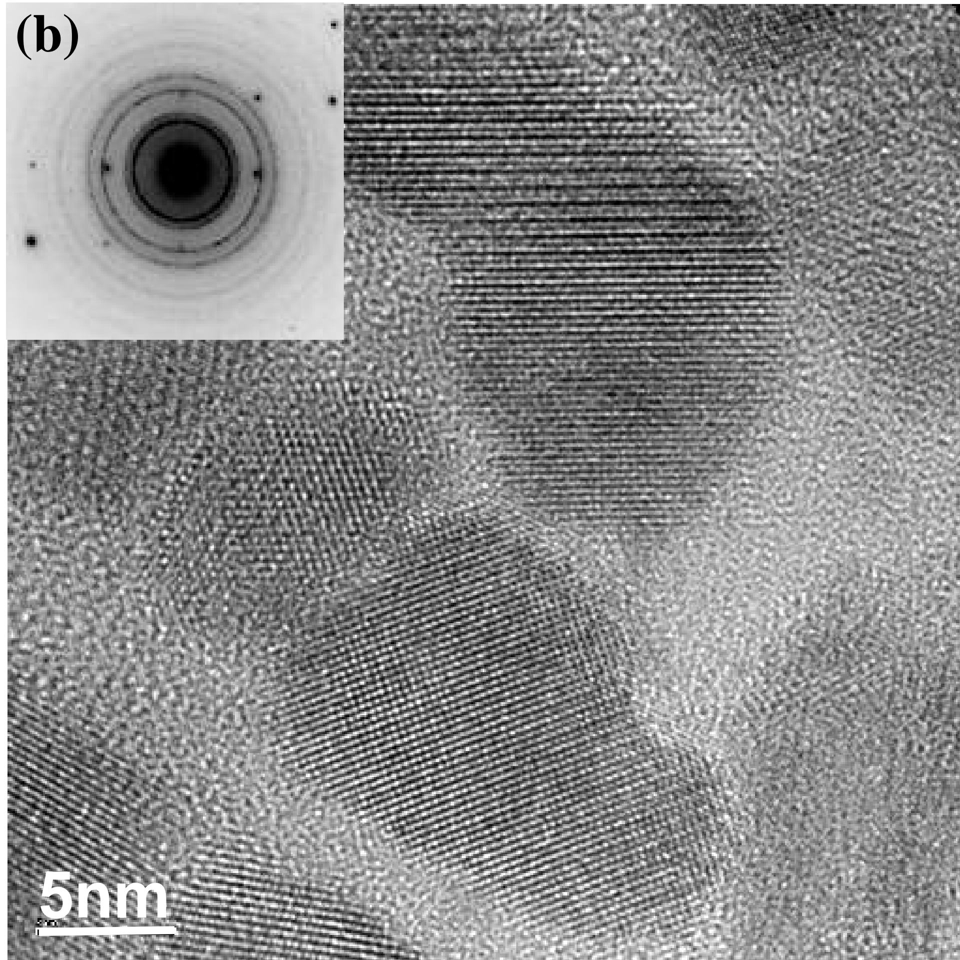

Yang *et al.*, Figure 2b

Figure 2 (c)

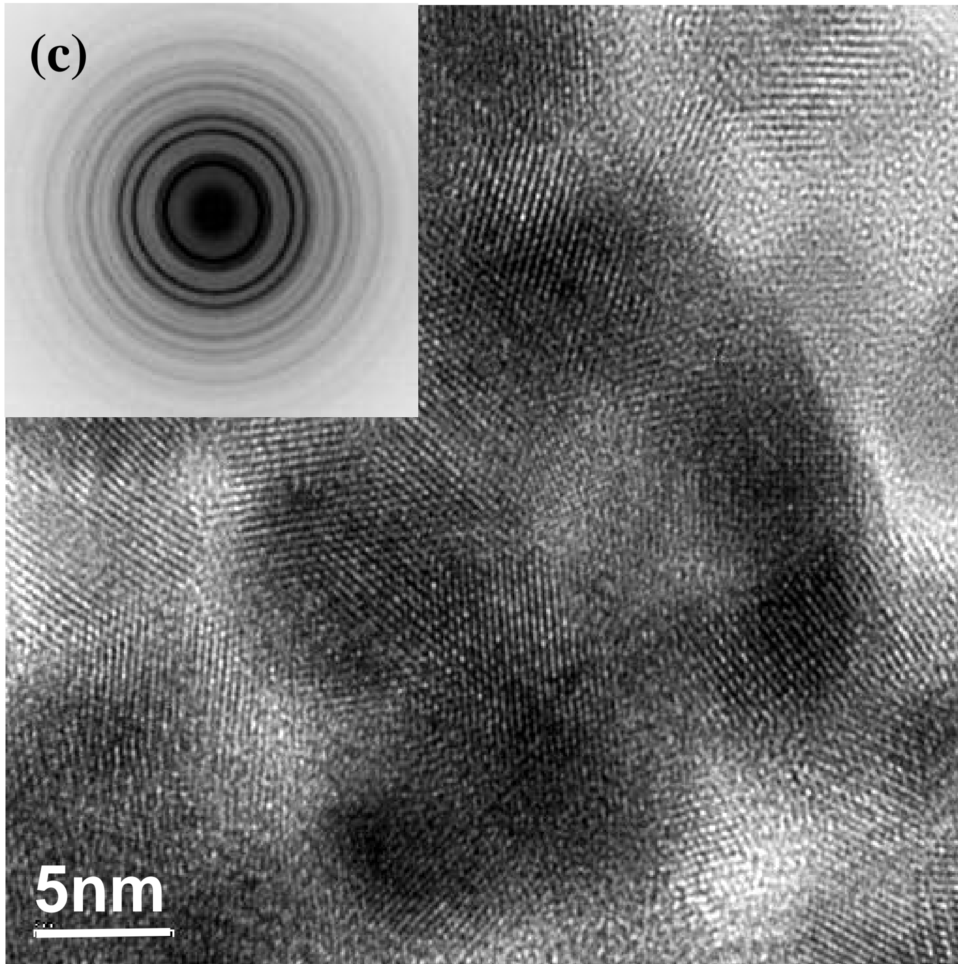

Yang *et al.*, Figure 2c

Figure 2 (d)

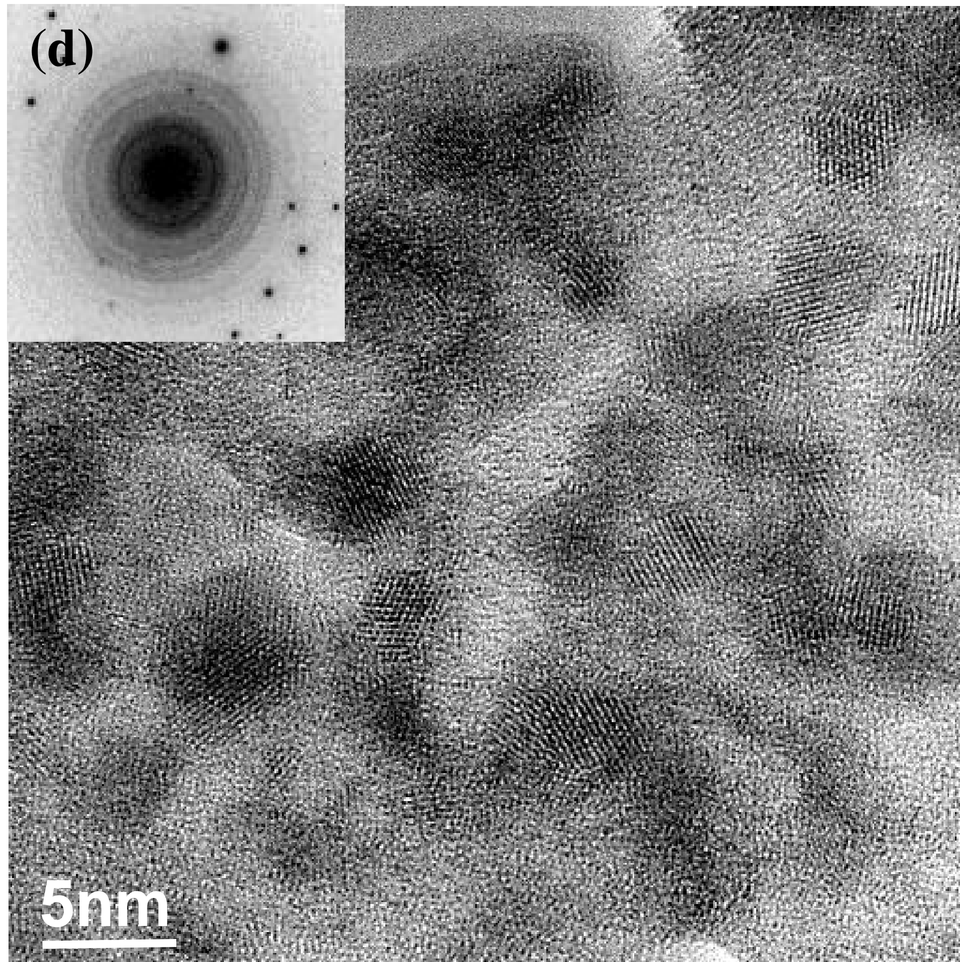

Yang *et al.*, Figure 2d

Figure 2 (e)

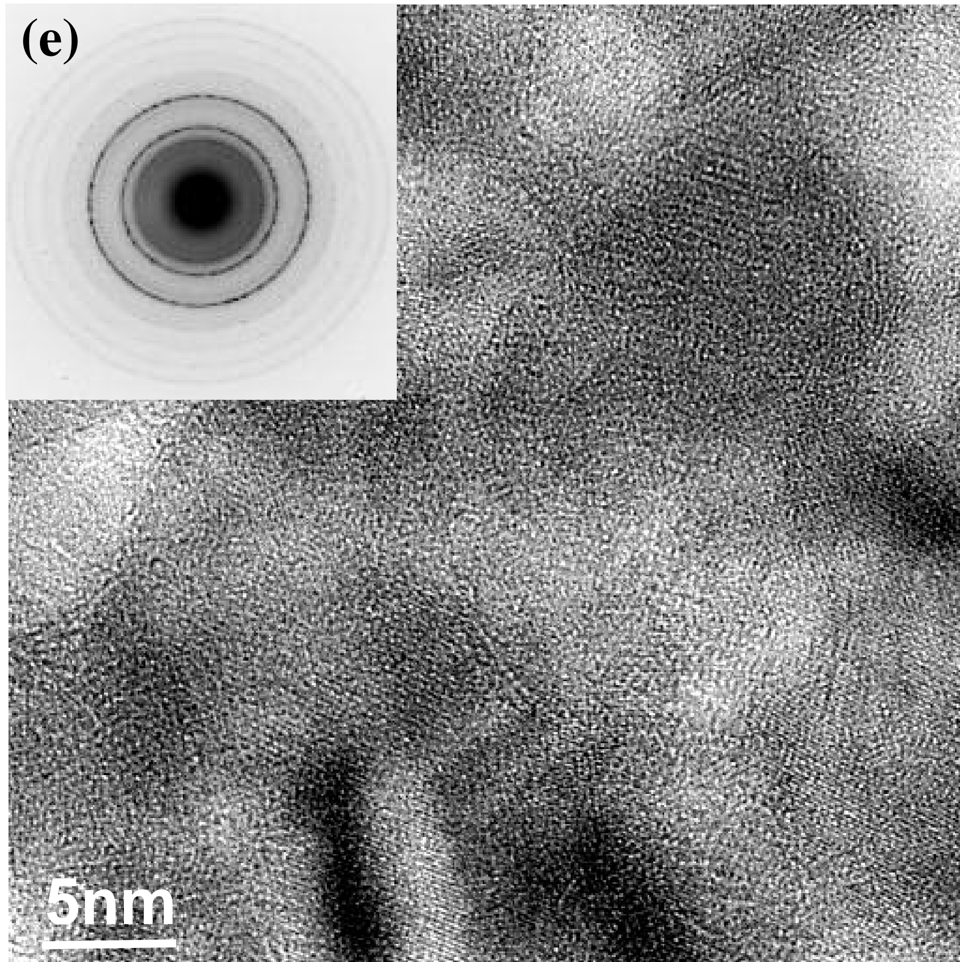

Yang *et al.*, Figure 2e

Figure 3

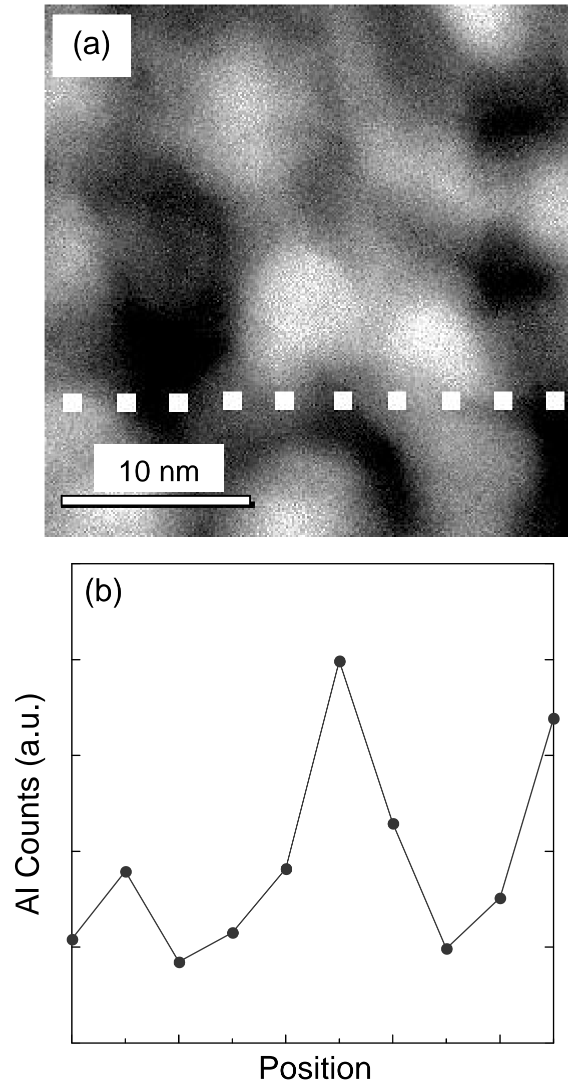

Yang *et al.*, Figure 3